nature physics

Article

https://doi.org/10.1038/s41567-023-02334-7

Long-lived valley states in bilayer graphene quantum dots

Received: 2 April 2023

Accepted: 14 November 2023

Published online: 17 January 2024

Check for updates

Rebekka Garreis[1,4] ✉, Chuyao Tong[1,4] ✉, Jocelyn Terle[1], Max Josef Ruckriegel[1], Jonas Daniel Gerber[1], Lisa Maria Gächter[1], Kenji Watanabe[2], Takashi Taniguchi[3], Thomas Ihn[1], Klaus Ensslin[1] & Wei Wister Huang[1]

Bilayer graphene is a promising platform for electrically controllable qubits in a two-dimensional material. Of particular interest is the ability to encode quantum information in the valley degree of freedom, a two-fold orbital degeneracy that arises from the symmetry of the hexagonal crystal structure. The use of valleys could be advantageous, as known spin- and orbital-mixing mechanisms are unlikely to be at work for valleys, promising more robust qubits. The Berry curvature associated with valley states allows for electrical control of their energies, suggesting routes for coherent qubit manipulation. However, the relaxation time of valley states—which ultimately limits these qubits' coherence properties and therefore their suitability as practical qubits—is not yet known. Here we measure the characteristic relaxation times of these spin and valley states in gate-defined bilayer graphene quantum dot devices. Different valley states can be distinguished from each other with a fidelity of over 99%. The relaxation time between valley triplets and singlets exceeds 500 ms and is more than one order of magnitude longer than for spin states. This work facilitates future measurements on valley-qubit coherence, demonstrating bilayer graphene as a practical platform hosting electrically controlled, long-lived valley qubits.

Bilayer graphene (BLG) offers unique opportunities as a host material for spin qubits[1,2]. These include weak spin–orbit interactions[3,4] and natural nuclear-spin concentrations as low as 1.1% (compared to 4.7% in Si), which can be further improved by isotopic purification[5]. Two-dimensional (2D) materials allow for the realization of smaller transistors[6] and possibly more strongly coupled quantum devices, as compared to bulk materials.

In addition, the symmetry of the hexagonal Bravais lattice of BLG gives rise to a valley degeneracy, which behaves analogously to spins[7–10]. This unique valley degeneracy in BLG with electrically tunable valley *g*-factor[8] provides an additional degree of freedom to realize and manipulate qubits. In particular, there is the prospect of realizing highly robust qubits with valley states. Whereas charge qubits couple to electric fields and spin qubits to magnetic fields, valley qubits consist of two degenerate states with the same charge distribution and the same spin configuration, but differ in their locations in reciprocal space. Theories have proposed various intervalley scattering mechanisms, requiring a short-range event on the scale of the lattice period[11,12]. Hence, for sufficiently low atomic defect density, the valley lifetimes are expected to be limited not by intrinsic mixing mechanisms such as phonon-mediated spin–valley coupling but by the finite size of the dot ultimately breaking translational invariance, similar to that previously discussed for transition metal dichalcogenides[13]. So far, however, only very short valley lifetimes have been observed, not in graphene but in optically addressed valley qubits in other 2D materials[14].

[1]Laboratory for Solid State Physics, ETH Zurich, Zurich, Switzerland. [2]Research Center for Functional Materials, National Institute for Materials Science, Tsukuba, Japan. [3]International Center for Materials Nanoarchitectonics, National Institute for Materials Science, Tsukuba, Japan. [4]These authors contributed equally: Rebekka Garreis, Chuyao Tong. ✉e-mail: garreisr@phys.ethz.ch; ctong@phys.ethz.ch

https://doi.org/10.1038/s41567-023-02334-7

The development of BLG quantum dot devices has made rapid progress in recent years[7,15–18], with the demonstration of high quality and controllability[8,19] and the discovery of intriguing physics[3,4,9,20,21], such as switchable Pauli spin and valley blockade in coupled double quantum dots[22], as well as the realization of high-quality charge-sensing technology[23,24]. In recent experiments, we found spin-relaxation times T_1 of up to 50 ms measured with the single-shot Elzerman readout technique[25] in a single quantum dot[26], comparable with values from other semiconductor quantum dot systems[27], such as in III–V[28–30], silicon-based[31–34] and germanium-based[35] heterostructures. Here we demonstrate single-shot readout with both spin and valley Pauli blockade[36,37] in gate-defined BLG double quantum dots and the associated measurement of characteristic spin and valley relaxation times T_1 between spin- or valley-triplet and singlet states. Using a property unique to BLG, we can select between spin- or valley-blockade regimes by choosing appropriate perpendicular magnetic fields[22]. The spin-T_1 time is measured to be up to 60 ms at $B_\perp = 700$ mT, corroborating our recent findings in single quantum dots[26]. By increasing the interdot tunnel coupling, the spin-T_1 time is reduced. We observe outstandingly long valley-T_1 times, longer than 500 ms at $B_\perp = 250$ mT. Unlike in the relaxation of spin states, intervalley relaxation times are found to be robust against variation of the interdot tunnel coupling strength. This valley lifetime is comparable with the state-of-the-art spin singlet-triplet T_1 measured in Si/SiGe and Si/SiO_2 and an order of magnitude longer than their T_1 reported at such low magnetic field[38,39].

The BLG double quantum dots studied here are defined by electrostatic gating in the sample shown in Fig. 1a (for details on sample fabrication and quantum dot tuning, see Methods). In one channel, we define the two quantum dots L and R underneath their respective plunger gates (dark red) with voltages V_L and V_R. The dot–lead and interdot tunnel couplings are controlled individually by the left, right and middle barrier gate (light red) voltages $V_{LB,RB}$ and V_{MB}, respectively. Separated by a depletion region, a third quantum dot (labelled 'detector' in Fig. 1a) formed in the neighbouring channel is controlled by the middle and right plunger-gate (blue) voltages V_{DM} and V_{DR}. This dot serves as a charge sensor, as it is capacitively coupled to dots L and R, more strongly to the left than to the right dot. A change in the double-dot charge configuration constitutes a discrete change of the electrostatic environment of the sensor dot, giving rise to a step in V_{det}, the voltage measured across the detection channel when applying a constant current bias[23]. The sensor dot is tuned to be at the rising or falling edge of a conductance resonance for optimized sensitivity and detection bandwidth[24].

We tune the double dot to the previously studied[22] two-electron configuration near the (1, 1)–(0, 2) charge degeneracy, where (N_L, N_R) labels the number of electrons in the left and in the right dot. With long integration time (20 ms) in the detector circuit, the relevant charge states manifest themselves as discrete values of V_{det}, as shown in the charge stability map (Fig. 1b). All four charge states (1, 1), (0, 2), (0, 1) and (1, 2) can be clearly distinguished. For single-shot readout, we fix V_L and V_R to an operating point and apply voltage pulses $V_{pulse,L}$ and $V_{pulse,R}$ to the left and the right plunger gates (see Fig. 1a for the schematic circuit). We collect real-time data during the pulsed experiments at a sampling rate of 27.5 kHz.

Figure 1b,c depicts the readout protocol for measuring inelastic relaxations between (1, 1) and (0, 2) states. Before describing which quantum states are addressed in the two charge configurations, we first discuss this protocol as an example to explain our general measurement scheme. Starting at the unload point U with a (0, 1) state, we first prepare a (1, 1) state by pulsing from U to the load (L) configuration within time t_L, which is much longer than the dot–lead tunnelling time, so that an electron can tunnel into the left dot with high fidelity while the (0, 2) level remains above the Fermi energy of the leads. We then pulse to an anchor point (A), where both the (1, 1) and the (0, 2) states

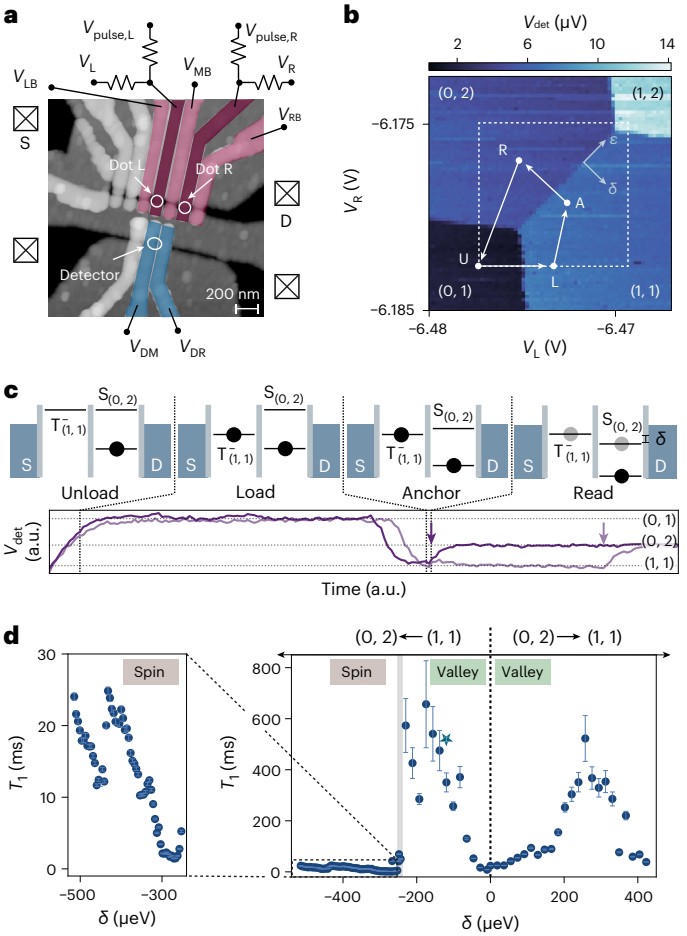

Fig. 1 | Pulse protocol used to determine spin and valley relaxation times. **a**, False-colour atomic force microscopic image of the device. The double quantum dot is formed underneath gates L and R (dark red), with tunable tunnel barrier gates (light red). In the other channel, a detector quantum dot with the middle and right detector plunger gates DM and DR is capacitively coupled to the double quantum dots and serves as a charge sensor. **b**, Charge stability map probed with detector signal V_{det} measured across the current-biased detector channel, around the (1, 1)–(0, 2) charge transition. Axes of total energy ϵ and energy detuning δ are marked. The dashed square with a side length of 8 mV marks the experimentally accessible pulse window, limited by the amplitude of the pulse generator. **c**, Spin and valley pulsing protocol for (1, 1) → (0, 2) with corresponding exemplary time traces. The gate position for each phase is marked in **b**. Starting from the (0, 1) state in unload (U), we pulse to the load position (L) slower than the dot–lead tunnel rate to prepare a (1, 1) state. We then pulse to the anchor point (A) slower than the line-bandwidth of the order of 100 μs, before pulsing to the read location (R). In the read phase, the system is energetically preferred to transfer to (0, 2), but is forbidden to do so by mismatching quantum numbers between triplet (1, 1)T⁻ and singlet (0, 2)S, unless a relaxation event occurs (indicated by purple arrows in the time traces). **d**, Characteristic spin and valley relaxation times T_1 measured at perpendicular magnetic field $B_\perp = 250$ mT along the δ axis. Valley T_1 values exceeding 500 ms are measured, much longer than the measured spin $T_1 \approx 10$ ms. Error bars correspond to the standard deviation of the calculated T_1. The star marks measurements with a read time of 1.5 s.

are well below the Fermi energy in the leads, with (1, 1) remaining in the ground state. Subsequently, we pulse quickly (bandwidth-limited to the order of 10 kHz) to the read position (R), where the (0, 2) state is lower in energy than (1, 1). The electron in the left dot is now energetically allowed to relax into the right dot while releasing its excess energy into the environment. We wait at this position for a time t_R before returning to the unload point U. An inelastic transition between the (1, 1) and the (0, 2) state happening within the time interval t_R is detected in real

https://doi.org/10.1038/s41567-023-02334-7

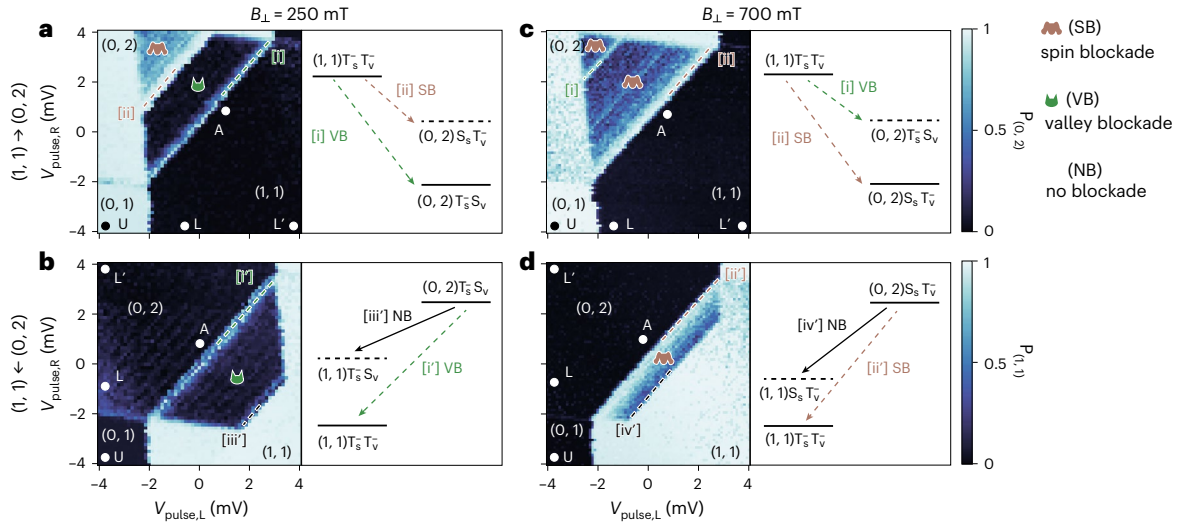

Fig. 2 | Probability of occupation in (0, 2) and (1, 1) states during the read phase and schematics showing the relevant states and transitions. **a**, Probability (left) and transitions (right) for pulsing from (1, 1) → (0, 2) at $B_\perp$ = 250 mT, while loading and anchoring at location L′. For (1, 1) → (0, 2) at $B_\perp$ = 250 mT, the strong valley blockade from (1, 1)$T_s^-T_v^-$ to the valley-mismatched ground state (0, 2)$T_s^-S_v$ is replaced by the weaker spin blockade to the spin-mismatched excited state (0, 2)$S_sT_v^-$ at [ii]. (The green and brown symbols label regions of valley and spin blockade, respectively, shown by the low occupation probability of the target states shown in the dark blue of the probability scale. Dashed lines indicate relevant state alignments. For the rest of the measurements, loading is performed at location L and anchoring at A.) **b**, As in **a**, for pulsing from (0, 2) → (1, 1) at 250 mT. (The parenthesized comments in **a** apply also to **b**, **c** and **d**.) **c**, As in **a**, for pulsing from (1, 1) → (0, 2) at $B_\perp$ = 700 mT. At $B_\perp$ = 700 mT, the ground-state spin blockade cannot be lifted by the stronger excited-state valley blockade at [i]. **d**, As in **c**, for pulsing from (0, 2) → (1, 1) at $B_\perp$ = 700 mT.

time. Figure 1c shows two exemplary time traces, with the inelastic transitions occurring at different times (purple arrows). Repeating this pulse sequence at least 10,000 times, we obtain the statistical distribution of the inelastic relaxation times, from which we extract the average relaxation time T_1. A similar scheme with points L and A in the (0, 2) and R in the (1, 1) region is applied for pulsing from an initial (0, 2) into the (1, 1) charge configuration for measuring the T_1 time of (0, 2) → (1, 1) transitions.

To select the specific quantum states between which we wish to measure the T_1 time, we apply a magnetic field perpendicular to the graphene plane[20,22,40,41] and study the relaxation between Pauli-blockaded valley and spin states at $B_\perp$ = 250 mT and 700 mT, respectively. In both cases, the lowest-energy (1, 1) states are valley- and spin-polarized (valley-triplet T_v^- and spin-triplet T_s^- state).

At $B_\perp$ = 250 mT, the (0, 2) ground state is a valley-singlet S_v spin-triplet state T_s^-; the (1, 1) ↔ (0, 2) transitions are therefore valley blockaded. At $B_\perp$ = 700 mT, the (0, 2) ground state has turned into a valley-polarized (valley-triplet T_v^-) spin-singlet state, such that the (1, 1) ↔ (0, 2) transitions are spin blockaded.

Figure 1d shows the main result of this paper for the T_1 times measured at $B_\perp$ = 250 mT as a function of detuning δ of the read position R from the charge transition line (orientation of the δ axis marked in Fig. 1b). At sufficiently small detuning $-250 < \delta < 420$ μeV, a valley flip is required to lift the valley blockade, so that the resulting T_1 times can be identified with the valley relaxation time. We observe exceptionally long relaxation times of $T_1 > 500$ ms, demonstrating that the valley states are remarkably long-lived in this double quantum dot system. This suggests that valley flips are suppressed within the dot and also during tunnelling, indicating that valley states are highly suitable for qubit operation. At $\delta < -250$ μeV, the (0, 2) excited state with valley-triplet spin-singlet character is lower in energy than the (1, 1) ground state and the valley blockade can therefore be circumvented with a spin-flip transition to this state. In this regime, we measure the spin-relaxation time $T_1 \leq 25$ ms, which is an order of magnitude shorter than the valley relaxation time, but still comparable with values observed in other semiconductor quantum dot systems and sufficiently long for high-fidelity qubit operation and readout.

As an illustration of the details that lead to and go beyond the results presented in Fig. 1d, we show in Fig. 2 data obtained from pulse cycles at $B_\perp$ = 250 mT and 700 mT. We pulsed during the load phase from U deep into a,c the (1, 1) or b,d the (0, 2) configurations at locations L′ (marked in Fig. 2) loading predominantly the respective ground states. Then, fixing U and L′ and anchoring at L′, we raster-scanned the read configuration R over the region marked with the dashed square in Fig. 1b and repeated at least 50 pulse cycles for each point. The V_{det} signal averaged over the read time t_R and over all the pulse cycles reflects the probabilities $P_{(0,2)}$ (Fig. 2a,c) and $P_{(1,1)}$ (Fig. 2b,d) at R[36,42]. The resulting normalized probability maps are shown in Fig. 2a,b for $B_\perp$ = 250 mT and Fig. 2c,d for $B_\perp$ = 700 mT. For a detailed description of the relevant (1, 1) and (0, 2) states involved and their evolution in the magnetic field $B_\perp$, see Supplementary Information section A.

At $B_\perp$ = 250 mT (Fig. 1d and 2a,b), the (0, 2) ground state is the valley-singlet spin-triplet $T_s^-S_v$. The bundle of (1, 1) states (containing all spin-triplet and -singlet states, split off by the Zeeman energy and zero field spin–orbit splitting (Δ_{SO})) with polarized valleys T_v^- is lower in energy than the bundle of (1, 1)S_v/T_v^0 by $g_v\mu_B B_\perp$, where μ_B is the Bohr magneton and g_v, approximately 20, is the dot-geometry-dependent valley g-factor, as the energies of the valley states couple to a perpendicular magnetic field, similar to the Zeeman effect for spins. Thus, in Fig. 2a, a strongly blockaded region (green label) is observed for (1, 1) → (0, 2), where the system remains mostly in (1, 1)T_v^- during reading (26 ms), since its transition [i] to the ground state (0, 2)S_v is valley blockaded. At large enough $|\delta|$, when the (0, 2)$S_sT_v^-$ excited state becomes accessible, the spin-blockaded transition [ii] to this state can circumvent the valley-blockaded transition [i] at the cost of a spin-flip. Because the valley-blockaded region (green label) is lifted by spin blockade (brown label) on transition [ii] with shorter yet still finite relaxation time, we conclude that spin flips occur more frequently than valley flips. The (0, 2) excited state, with matching quantum numbers $T_s^-T_v^-$ and able to lift both spin and valley blockade, occurs at much higher energies[40]. A strongly blockaded region (green label in Fig. 2b)

https://doi.org/10.1038/s41567-023-02334-7

is also observed for (0, 2) → (1, 1), since transition [i′] from the (0, 2) ground state S_v to the (1, 1) ground state T_v^- is valley blockaded. This blockade is completely lifted at large enough $|\delta|$ at [iii′], giving access to the excited state $(1,1)T_S^-S_v$ with matching quantum numbers. We observe valley blockade stemming from the same set of states and transitions at even lower magnetic field, as low as at $B_\perp = 20$ mT (see Supplementary Information section C).

With this scenario in mind, we move to $B_\perp = 700$ mT (Fig. 2c,d), where the (0, 2) ground state changes to $(0,2)S_sT_v^-$, due to T_v^- being lowered in energy by the coupling of the valleys to $B_\perp$. The [i] valley- and [ii] spin-blockaded transitions thus reverse their order in energy relative to the scenario at $B_\perp = 250$ mT. In Fig. 2c, the transition [ii] from the loaded $(1,1)T_S^-T_v^-$ to the spin-mismatched ground state $(0,2)S_sT_v^-$ gives rise to a spin-blockaded region (brown label). Resonance [i] at finite $|\delta|$ appears, since the now excited valley-mismatched state $(0,2)T_S^-S_v$ is accessible in energy. However, unlike at $B_\perp = 250$ mT, this excited state does not lift the spin blockade, since valley flips occur more slowly than spin flips. The spin-blockaded region (brown label) in Fig. 2d is much smaller for (0, 2) → (1, 1), because the (0, 2) ground state $T_S^-S_v$ is spin blockaded and cannot proceed to the ground state $(1,1)T_S^-T_v^-$ until access to the excited state $(1,1)S_sT_v^-$ lifts the spin blockade completely at [iv′], $g_s\mu_B B_\perp + \Delta_{SO}$ away in $|\delta|$, where $g_s = 2$ is the spin g-factor and $\Delta_{SO} \approx 60$ μeV is the zero-field Kane–Mele splitting[3,4].

For the quantitative measurement of T_1 times, we choose load locations L in the probability maps in Fig. 2a that only load the respective ground states while avoiding the excited states. We choose unload and load times t_U and t_L to be longer than the dot–lead tunnelling rate; we choose the time t_A spent at the anchor point A to be longer than the rise time of our pulse lines at the order of 100 μs; and we choose read time t_R to be reasonably long compared to the probed relaxation times. Examples of time traces for (1, 1) → (0, 2) spin relaxation at 700 mT (at $\delta = -180$ μeV, marked by an arrow in Fig. 4b) are shown in Fig. 3a, left, with $t_R = 100$ ms, where registered relaxation events are indicated by arrows. We show the distribution of relaxation times for 10,000 repeated pulse cycles in Fig. 3b, left, plotted on a logarithmic scale; this distribution is well described by an exponential decay e^{-t/T_1}, with T_1 being the characteristic spin-relaxation time. To extract T_1, we perform a Bayesian analysis based on the exponential model e^{-t/T_1} using the average relaxation time $\langle t \rangle$ within the read-time interval $[t_0, t_1]$ as the relevant statistics. The finite read-time interval removes events occurring before the detection read-window opens at t_0 and those after t_1, the end of the read-window, with the detection window subtracted (see Methods for a detailed explanation of the analysis performed). The data as extracted by this method are well fitted by an exponential decay with $T_1 = 34 \pm 1$ ms.

The long-lived valley states are found for (1, 1) → (0, 2) by measuring valley relaxation at $B_\perp = 250$ mT (at $\delta = -100$ μeV, marked by an arrow in Fig. 4a) with read time $t_R = 1.5$ s, much longer than that for spin relaxation, to capture most relaxation events within the readout window. Examples of time traces are shown in Fig. 3a, right, with the distribution of 10,000 repeated pulse cycles plotted in Fig. 3b, right. The valley-relaxation data are also well fitted by an exponential decay, evaluating to a characteristic valley-relaxation time of $T_1 = 354 \pm 5$ ms, in this example.

We now evaluate quantitatively the valley and spin readout fidelities in our experiment. We prepare $(1,1)T^-$ with a probability of roughly 50% at the beginning of the read phase. when plotting histograms of detector voltage V_{det} during the read phase, well-separated peaks corresponding to (1, 1) and (0, 2) charge states are seen, as shown in Fig. 3c,e. We follow the framework introduced in Barthel et al.[43] to model the distribution that includes the effect of a finite relaxation time T_1 and find an overall fidelity of 99.9727(17)% for the valleys. The shoulder in the lower histogram peak in Fig. 3c results from charge instabilities close to the detector influencing its asymmetry sensitivity and thus shifting both the spin singlet and triplet levels with respect to zero, but by a different amount (see Supplementary Information section D). The charge instability could be avoided by more accurate tuning. We calculate the model function for each singlet peak using the mean and variance of a Gaussian fit to extract lower bounds for the fidelity of 99.9033(18)% (solid) and 99.80(3)% (dashed) for the spins. We plot the evolution of the infidelity with the length of the considered read phase in Fig. 3d and find that our signal-to-noise ratio does not need improvement to obtain higher fidelity, but that the finite relaxation time T_1 limits the fidelity, which decreases for longer t_{int} for both spins and valleys. The decrease of fidelity with t_{int} occurs more quickly for spins, due to the shorter T_1.

The characteristic relaxation times T_1 of valley and spin states were measured as a function of detuning δ (see Fig. 1b) by repeating the procedure described above. For valley relaxation, we chose a read time of $t_R = 140$ ms for shorter measurements and compensated the shorter read time by acquiring many more samples, 36,000 pulse cycles instead of 10,000 (see Methods for a more detailed discussion on this approach). The results are summarized in Fig. 4. The blue star marks the single measurement with longer read time in the valley-blockaded regime presented in Fig. 3. It matches well with the T_1 extracted from

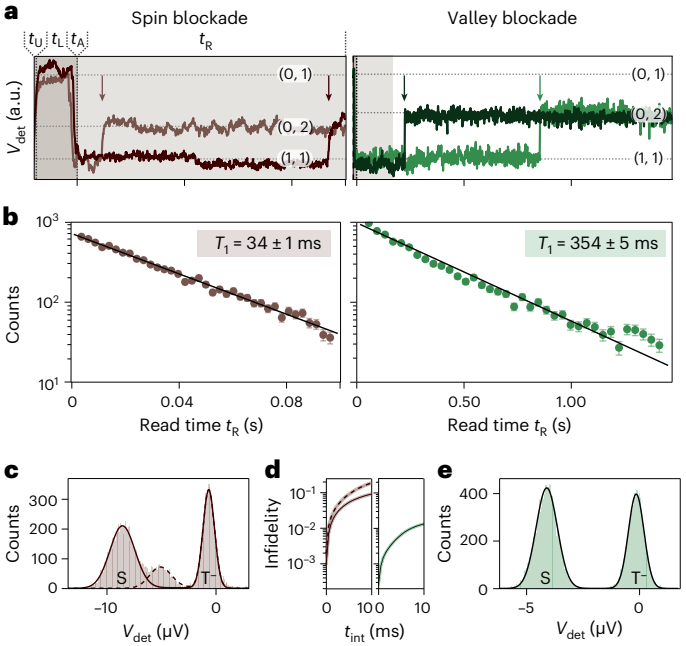

Fig. 3 | Extracting characteristic relaxation times T_1 of spins and valleys for (1, 1)T → (0, 2)S. a, Exemplary time traces with arrows marking relaxation events for spins on the left and for valleys on the right. **b**, Distribution of relaxation times for 10 000 pulse cycles, with T_1 calculated by solving for the ansatz e^{-t/T_1} with average relaxation time $\langle t \rangle$. Error bars correspond to the standard deviation of the binomial distribution of the number of counts. **c**, Distribution of V_{det} during the first 1 ms of the read phase. The $(1,1)T^-$ probability at the beginning of the read phase is roughly 50%. To describe the distribution, we follow ref. 43 to include the finite relaxation time during the read phase. We evaluate the two singlet peaks individually with $\mu_{S,1} = -8.54$ μV, $\sigma_{S,1} = 1.14$ μV, $\mu_{S,2} = -5.07$ μV, $\sigma_{S,2} = 0.99$ μV, $\mu_{T-,1} = -0.64$ μV, $\sigma_{T-,1} = 0.53$ μV, $T_1 = 34$ ms and $\tau_M = 1$ ms. **d**, Measured infidelity as a function of the integration time t_{int} of the read phase. For long integration times the relaxation lowers the fidelity. We find an overall maximum fidelity of 99.80% for spins (lower bound) and 99.97% for valleys. Shaded regions of each line indicate one standard deviation. **e**, As in **c**, for valleys. We find $\mu_S = -4.11$ μV, $\sigma_S = 0.47$ μV, $\mu_{T-,1} = -0.15$ μV, $\sigma_{T-,1} = 0.34$ μV, $T_1 = 354$ ms and $\tau_M = 1$ ms. The spin data (**c** left) is acquired at $B_\perp = 700$ mT, the valley data (right) at $B_\perp = 250$ mT, for detuning values marked by arrows in Fig. 4, while loading at L as marked in Fig. 2 to ensure loading of the (1, 1) ground state and anchoring at A.

https://doi.org/10.1038/s41567-023-02334-7

shorter measurements. We see clearly a drop of the apparent T_1 time by roughly an order of magnitude because the detuning causes a change from valley to spin blockade at $\delta = -240$ μeV, for transition [ii] in Fig. 2a. Both spin and valley T_1 times show complex behaviour as a function of detuning. Our findings align with a similar trend of non-monotonic detuning dependence that was highlighted in ref. 36. It is important to note that the detuning range under scrutiny in our research is substantialy offset from the (2, 1) and (1, 0) charge states. This implies that thermal relaxation may not be the primary factor at play. We attribute the dips in relaxation time partially to the coupling to excited states transitioning from the (1, 1) triplet to the (0, 2) charge state. These distinct peaks of increased relaxation, or hotspots, correspond to situations of maximal overlap between these states. In such cases, phonon interactions facilitate the process, pushing the relaxation times toward a minimum. When moving away from these anti-crossings, the relaxation time exhibits a recovery to its maximum values.

We also adjusted the strength of the tunnel coupling between the quantum dots to probe its influence on the measured spin and valley relaxation rates. Any such dependence potentially contains information relevant to future research to identify the relaxation mechanisms. Figure 4a,b shows measured relaxation times at $B_\perp = 250$ mT and 700 mT, respectively, as a function of detuning with T_1 times plotted on a logarithmic scale for two different voltages V_{MB} applied to the tunnel barrier gate between the two dots, resulting in stronger (red) and weaker (blue) interdot coupling strength, but both within the overall weak-coupling regime. Spin- and valley-blockaded regions are labelled in accordance with the discussion of Fig. 2, separated by transition [ii]. We mark by arrows in Fig. 4 the locations of δ at which the examples in Fig. 3 are taken. We notice that the valley T_1 appears to be independent of interdot coupling, whereas the spin T_1 decreases consistently at both 250 mT and 700 mT by an order of magnitude from around 30 ms to 1 ms for stronger interdot coupling. This observation indicates that the mechanisms assisting spin relaxation evidently depend on interdot tunnelling, potentially hinting toward the involvement of momentum-dependent spin–orbit interactions[44]. For valley relaxation, such mechanisms are clearly not the main contributors. Despite the shift of excited-state resonances due to the spin- and valley-state coupling to $B_\perp$, no notable influence of $B_\perp$ on the measured T_1 times can be concluded (for more details, see Supplementary Information section E).

We probe the coupling of resonant (1, 1) and (0, 2) states in the spirit of Landau–Zener tunnelling experiments. In Fig. 2, peaks of probabilities are seen when states align in energy (marked by dashes), indicating finite coupling between the aligned states, which lifts the Pauli blockade. For the data presented in Figs. 1–4, we have pulsed from the anchor point A to the read position R as fast as permitted by our line-bandwidth, on the order of 10 kHz permit. In further experiments, we altered the transit time from A to R while keeping the read position R constant, thereby varying the energy sweep rate υ. We repeated the procedure for 2,000 pulse cycles at each sweep rate and registered events where transfer from (1, 1) to (0, 2) happens diabatically. In Fig. 5a,c, the probability distribution $P_{triplet}$ of retaining (1, 1)T after passing through the avoided crossing is plotted on a logarithmic scale against $1/\upsilon$ for the two magnetic fields, Fig. 5a showing results at $B_\perp = 250$ mT and Fig. 5c the results at $B_\perp = 700$ mT, probing valley and spin blockade, respectively. The same experiment was performed for stronger (red) and weaker (blue) interdot tunnel coupling. In all cases, the data are compatible with the exponential dependence $P_{LZ} = \exp(-2\pi\Delta^2/\upsilon\hbar)$ predicted by the Landau–Zener formula, where 2Δ is the minimum energy splitting between the states. In agreement with the data shown in Fig. 4, intervalley coupling appears to be insensitive to the interdot tunnel coupling, whereas spin coupling clearly increases for stronger interdot tunnel coupling.

For a quantitative analysis of the data, we look at the level schemes depicted in Fig. 5b,d. Here, the relevant (1, 1) triplet states marked in black and the (0, 2) singlet states in green (valley singlets) or brown

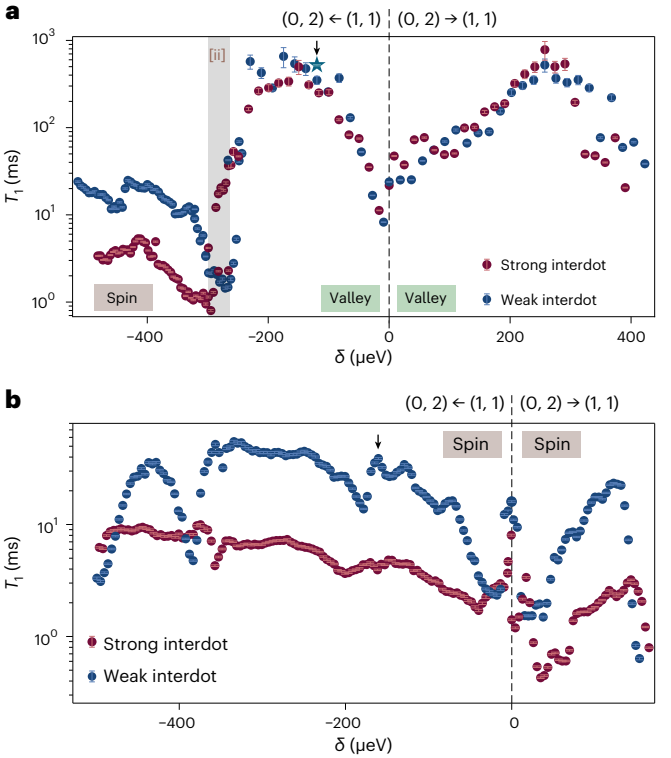

Fig. 4 | Spin and valley T_1 times with weaker and stronger interdot couplings. **a**, Spin and valley T_1 measured along the δ axis at $B\perp = 250$ mT, with weaker (blue) and stronger (red) interdot couplings. Error bars (frequently within the data marker) correspond to the standard deviation of the calculated T_1. The star marks measurements with read time of 1.5 s. **b**, As for **a**, with $B\perp = 700$ mT. In **a** and **b**, spin- and valley-blockaded regions are labelled, with transition [ii] separating the two regions. When the electrochemical levels in the two dots are aligned, we observe a dip in T_1.

(spin singlets). At $B_\perp = 250$ mT, the initial state at point A belongs to a state of the (1, 1)T_V^- bundle (see inset of Fig. 5b), while the resulting state at point R is in the same (1, 1) bundle or in the (0, 2) bundle of states (green in Fig. 5b). The measured probability distribution $P_{triplet}$ is therefore a 'bundle' distribution potentially giving the coupling between the two crossing state bundles of distinct valley character. By contrast, at $B_\perp = 700$ mT, the distribution refers to the coupling between two distinct spin states, (1, 1)$T_S^-T_V^-$ and (0, 2)$S_sT_V^-$. We also note that all distributions in Fig. 5a,c seem to be double exponentials, with a fast decay rate at very small $1/\upsilon$ and a slower rate at larger $1/\upsilon$ (separated in the figure by vertical lines). To obtain a naïve estimate of the energy scales for the coupling of the involved states, we apply the Landau–Zener formula to both the fast and slow decay in all four traces. For the intervalley coupling Δ at $B_\perp = 250$ mT, we find the values 1.5 neV and 1.2 neV for weaker (blue in Fig. 5), and 1.6 neV and 1.2 neV for stronger (red) tunnel coupling (the two values corresponding to the two slopes of the double exponential). At $B_\perp = 700$ mT for spin states, we find 5.3 neV and 3.0 neV for weaker (blue) and 7.6 neV and 4.8 neV for stronger (red) interdot tunnel coupling. These values correspond to time scales $\hbar/\Delta$ of the order of a few hundred nanoseconds. For spins, the same measurement technique[45] gave a gap size of 60 neV for gallium arsenide[46] and 113 neV for silicon[47].

The double-exponential decay could arise from contributions of inelastic T_1 decay during the transit from point A to R, as well as the coherent Landau–Zener physics accounted for by the transition probability P_{LZ}. This scenario would tend to invalidate our naïve application of the Landau–Zener formula and make a more involved, possibly incoherent analysis necessary[48,49]. Furthermore, the energy scales

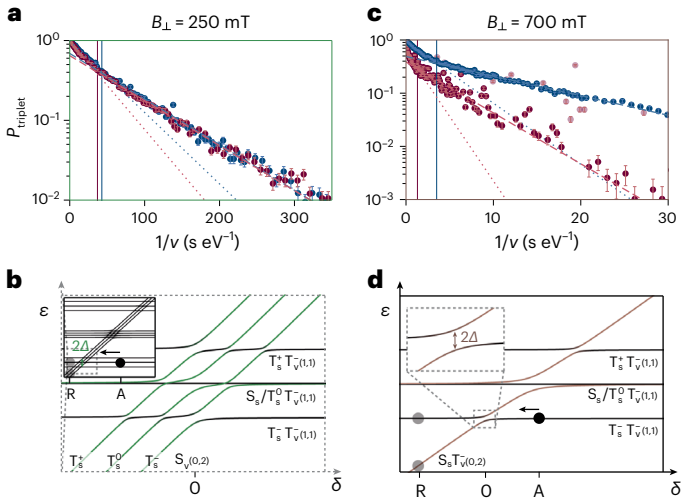

Fig. 5 | Probing the triplet T^- singlet S coupling Δ for valleys and spins using the Landau–Zener non-adiabatic transition probability $P_{LZ}=e^{(-2\pi\Delta^2/v\hbar)}$. **a**, The probability of non-adiabatic retention of the (1, 1) state $P_{triplet}$, at $B_\perp$ = 250 mT, starting from point A with (1, 1)T^- and after passing through the anti-crossing at various energy sweep rates v, adjusted by fixing the read position and altering the pulse time. **b**, Energy diagram of relevant (1, 1) and (0, 2) states corresponding to events in **a**. **c**, As in **a**, at $B_\perp$ = 700 mT. **d**, Energy diagram of relevant (1, 1) and (0, 2) states corresponding to events in **c**. For the data presented in **a** and **c**, 2,000 pulse cycles were performed for each sweep rate. The data points shown in transparent colour are excluded from the fit. Error bars correspond to the standard deviation of the binomial probability density distribution.

we extracted are extremely small, of the order of nanoelectronvolts, a factor of 1,000 smaller than the temperature of the experiment. One might therefore expect that interactions of the electronic states with other degrees of freedom in the device become relevant, with virtual transitions, phonons or charge noise being among the most obvious candidates. We therefore regard the extracted coupling values as upper bounds for the true 'intrinsic' values. The experimental evidence of an exponential dependence on $1/v$ remains a robust outcome of our experiment.

The spin T_1 times of up to 60 ms in our experiments compare well with recent experiments on single quantum dots using the Elzerman readout[26]. The impressively lengthy valley T_1 times of more than 500 ms, which we show to be robust against interdot tunnel coupling, open up interesting avenues for exploiting valley physics, and, together with the widely tunable valley g-factor, offer experimental schemes for electrically and coherently driven valley qubits. Our work raises the question of how valley qubits can be manipulated by experimentally accessible parameters. That the K-valleys are good quantum numbers relies on the translational invariance of the crystal. The electronic wave function in our dots extends over approximately 50 nm, comprising some 400 lattice constants; this means that translational invariance remains a good concept. As layers get thinner, especially the insulating hBN layers, and gate geometries smaller, it is conceivable that graphene quantum dots may be created that are much smaller and tunable in size, possibly allowing gate manipulation of the valley degrees of freedom. A practical concept for operation and coherent control of valley qubits in graphene requires a better understanding of the mechanisms limiting the valley (and spin) T_1 times as observed in our experiments. The next experimental steps will include measurements with radio frequency pulse lines, to observe T_2, the dephasing time—another crucial timescale for qubit operation—and of coherent valley oscillations in real time.

Online content

Any methods, additional references, Nature Portfolio reporting summaries, source data, extended data, supplementary information, acknowledgements, peer review information; details of author contributions and competing interests; and statements of data and code availability are available at https://doi.org/10.1038/s41567-023-02334-7.

References

1. Trauzettel, B., Bulaev, D. V., Loss, D. & Burkard, G. Spin qubits in graphene quantum dots. *Nat. Phys.* **3**, 192 (2007).
2. Hanson, R., Kouwenhoven, L. P., Petta, J. R., Tarucha, S. & Vandersypen, L. M. K. Spins in few-electron quantum dots. *Rev. Mod. Phys.* **79**, 1217 (2007).
3. Kurzmannet. A. et al. Kondo effect and spin-orbit coupling in graphene quantum dots. *Nat. Commun.* **12**, 6004 (2021); https://doi.org/10.1038/s41467-021-26149-3
4. Banszeruset, L. et al. Spin relaxation in a single-electron graphene quantum dot. *Nat. Commun.* **13**, 3637 (2022); https://doi.org/10.1038/s41467-022-31231-5
5. Chen, S. et al. Thermal conductivity of isotopically modified graphene. *Nat. Mater.* **11**, 203 (2012).
6. Liu, Y. et al. Promises and prospects of two-dimensional transistors. *Nature* **591**, 43 (2021).
7. Eich, M. et al. Spin and valley states in gate-defined bilayer graphene quantum dots. *Phys. Rev. X* **8**, 031023 (2018).
8. Tong, C. et al. Tunable valley splitting and bipolar operation in graphene quantum dots. *Nano Lett.* **21**, 1068 (2021).
9. Garreis, R. et al. Shell filling and trigonal warping in graphene quantum dots. *Phys. Rev. Lett.* **126**, 147703 (2021).
10. Recher, P., Nilsson, J., Burkard, G. & Trauzettel, B. Bound states and magnetic field induced valley splitting in gate-tunable graphene quantum dots. *Phys. Rev. B* **79**, 085407 (2009).
11. Pályi, A. & Burkard, G. Hyperfine-induced valley mixing and the spin-valley blockade in carbon-based quantum dots. *Phys. Rev. B* **80**, 201404 (2009).
12. Morpurgo, A. F. & Guinea, F. Intervalley scattering, long-range disorder, and effective time-reversal symmetry breaking in graphene. *Phys. Rev. Lett.* **97**, 196804 (2006).
13. Liu, G.-B., Pang, H., Yao, Y. & Yao, W. Intervalley coupling by quantum dot confinement potentials in monolayer transition metal dichalcogenides. *New J. Phys.* **16**, 105011 (2014).
14. Soni, A. & Pal, S. K. Valley degree of freedom in two-dimensional van der Waals materials. *J. Phys. D: Appl. Phys.* **55**, 303003 (2022).
15. Banszerus, L. et al. Gate-defined electron-hole double dots in bilayer graphene. *Nano Let.* **18**, 4785 (2018).
16. Eich, M. et al. Coupled quantum dots in bilayer graphene. *Nano Lett.* **18**, 5042 (2018).
17. Banszerus, L. et al. Single-electron double quantum dots in bilayer graphene. *Nano Lett.* **20**, 2005 (2020).
18. Eich, M. et al. Coulomb dominated cavities in bilayer graphene. *Phys. Rev. Res.* **2**, 022038 (2020).
19. Banszerus, L. et al. Electron-hole crossover in gate-controlled bilayer graphene quantum dots. *Nano Lett.* **20**, 7709–7715 (2020).
20. Kurzmann, A. et al. Excited states in bilayer graphene quantum dots. *Phys. Rev. Lett.* **123**, 026803 (2019).
21. Tong, C. et al. Three-carrier spin blockade and coupling in bilayer graphene double quantum dots. Preprint at *arXiv* https://doi.org/10.48550/arXiv.2211.04882 (2022).
22. Tong, C. et al. Pauli blockade of tunable two-electron spin and valley states in graphene quantum dots. *Phys. Rev. Lett.* **128**, 067702 (2022).
23. Kurzmann, A. et al. Charge detection in gate-defined bilayer graphene quantum dots. *Nano Lett.* **19**, 5216 (2019).

24. Garreis, R. et al. Counting statistics of single electron transport in bilayer graphene quantum dots. *Phys. Rev. Research* **5**, 013042 (2023).
25. Elzerman, J. M. et al. Single-shot read-out of an individual electron spin in a quantum dot. *Nature* **430**, 431 (2004).
26. Gächter, L. M. et al. Single-shot spin readout in graphene quantum dots. *PRX Quantum* **3**, 020343 (2022).
27. Stano, P. & Loss, D. Review of performance metrics of spin qubits in gated semiconducting nanostructures. *Nat. Rev. Phys.* **4**, 672 (2022).
28. Nakajima, T. et al. Coherence of a driven electron spin qubit actively decoupled from quasistatic noise. *Phys. Rev. X* **10**, 011060 (2020).
29. Cerfontaine, P., Botzem, T., DiVincenzo, D. P. & Bluhm, H. High-fidelity single-qubit gates for two-electron spin qubits in GaAs. *Phys. Rev. Lett.* **113**, 150501 (2014).
30. Nichol, J. M. et al. High-fidelity entangling gate for double-quantum-dot spin qubits. *npj Quantum Inf.* **3**, 3 (2017).
31. Xue, X. et al. Quantum logic with spin qubits crossing the surface code threshold. *Nature* **601**, 343 (2022).
32. Zajac, D. M. et al. Resonantly driven cnot gate for electron spins. *Science* **359**, 439 (2018).
33. Yoneda, J. et al. A quantum-dot spin qubit with coherence limited by charge noise and fidelity higher than 99.9%. *Nat. Nanotechnol.* **13**, 102 (2018).
34. Mills, A. R. et al. Two-qubit silicon quantum processor with operation fidelity exceeding 99%. *Sci. Adv.* **8**, eabn5130 (2022).
35. Hendrickx, N. W. et al. A four-qubit germanium quantum processor. *Nature* **591**, 580 (2021).
36. Johnson, A. et al. Triplet–singlet spin relaxation via nuclei in a double quantum dot. *Nature* **435**, 925 (2005).
37. Zheng, G. et al. Rapid gate-based spin read-out in silicon using an on-chip resonator. *Nat. Nanotechnol.* **14**, 742 (2019).
38. Prance, J. R. et al. Single-shot measurement of triplet-singlet relaxation in a Si/SiGe double quantum dot. *Phys. Rev. Lett.* **108**, 046808 (2012).
39. Yang, C. H. et al. Operation of a silicon quantum processor unit cell above one kelvin. *Nature* **580**, 350 (2020).
40. Möller, S. et al. Probing two-electron multiplets in bilayer graphene quantum dots. *Phys. Rev. Lett.* **127**, 256802 (2021).
41. Knothe, A. & Fal'ko, V. Quartet states in two-electron quantum dots in bilayer graphene. *Phys. Rev. B* **101**, 235423 (2020).
42. Churchill, H. O. H. et al. Relaxation and dephasing in a two-electron ^{13}C nanotube double quantum dot. *Phys. Rev. Lett.* **102**, 166802 (2009).
43. Barthel, C., Reilly, D. J., Marcus, C. M., Hanson, M. P. & Gossard, A. C. Rapid single-shot measurement of a singlet-triplet qubit. *Phys. Rev. Lett.* **103**, 160503 (2009).
44. Stepanenko, D., Rudner, M., Halperin, B. I. & Loss, D. Singlet-triplet splitting in double quantum dots due to spin-orbit and hyperfine interactions. *Phys. Rev. B* **85**, 075416 (2012).
45. Shevchenko, S., Ashhab, S. & Nori, F. Landau-Zener-Stückelberg interferometry. *Phys. Rep.* **492**, 1 (2010).
46. Petta, J. R., Lu, H. & Gossard, A. C. A coherent beam splitter for electronic spin states. *Science* **327**, 669 (2010).
47. Harvey-Collard, P. et al. Spin-orbit interactions for singlet-triplet qubits in silicon. *Phys. Rev. Lett.* **122**, 217702 (2019).
48. Shimshoni, E. & Stern, A. Dephasing of interference in Landau-Zener transitions. *Phys. Rev. B* **47**, 9523 (1993).
49. Krzywda, J. A. & Cywiński, L. Interplay of charge noise and coupling to phonons in adiabatic electron transfer between quantum dots. *Phys. Rev. B* **104**, 075439 (2021).

Methods

Sample geometry

The same device has been used before for the measurement of spin-relaxation times in ref. 26 and the evaluation of the full counting statistics in ref. 24. The fabrication of the van der Waals heterostructure follows the general procedure described in previous publications[7,15,50]. Stacked with the dry-transfer technique[51], it lies on a silicon chip with 280 nm surface SiO_2. From bottom to top, it is built up with a graphite back gate, a bottom hBN flake (31 nm) and a bilayer graphene flake capped with a top hBN flake (20 nm). The split gates (5 nm Cr and 20 nm Au) form two channels with a nominal width of 100 nm, with a separation gate of 150 nm width between them. The finger gates (5 nm Cr and 20 nm Au) have a width of 20 nm and a centre-to-centre distance of 85 nm. We use an aluminium oxide layer (30 nm) to separate the finger-gate layer from the split gates. Figure 1a shows a false-colour atomic force microscope image of the two layers of metal gates fabricated on top of the heterostructure. The split gates (dark grey) are used to form two conducting channels (black)[50]. For the measurements discussed in this paper, we use two finger gates (blue) to define a quantum dot based on a p–n junction[7,15] in the lower channel, which we utilize as a charge detector[23]. In the second channel we define two quantum dots below the gates marked in dark red colour and use the neighbouring gates (light red) to tune the tunnel coupling of the quantum dots to the leads and the interdot coupling[8,19]. All other gates are grounded.

Experimental setup

The sample is mounted in a dilution refrigerator with a nominal base temperature of 10 mK; in previous measurements, we extracted an electronic temperature of 50 mK in the same device and setup[24]. The detector dot is biased with a constant current of 10 pA using a low noise differential amplifier[52] and the voltage signal V_{det} is measured with a detector bandwidth of about 1 kHz and sampled at a rate of 27.5 kHz.

The d.c. voltage $V_{\mathrm{L(R)}}$ tuning the left (right) dot is combined with the pulse $V_{\mathrm{pulse,L(R)}}$ via two resistors at room temperature. The pulse lines to the sample have a rise time of 120 µs. The pulse sampling rate to generate the analogue pulse signal is 219.72 kHz.

Determination of T_1

The finite memory of our arbitrary waveform generator limits our maximum read time to $t_{\mathrm{R}} = 140$ ms. For the measurement presented in Fig. 3b, we choose a point in detuning, where we can set the read position to a point corresponding to applying $V_{\mathrm{pulse,L/R}} = 0$, that is, at the centre of the pulse window. This allows us to turn off the arbitrary waveform generator at the end of the pulse sequence and reach an arbitrarily long read phase. This approach is only possible for data points within a small range of detuning, because otherwise setting the centre of the pulse window at the read position means that the load and unload positions fall out of the pulse window. With this method, we choose a read phase of $t_{\mathrm{R}} = 1.5$ s, much longer than the extracted $T_1 = 354 \pm 5$ ms at this point. This allows us to confirm the exponential distribution of relaxation events.

For any other data presented here, the length t_{R} of the read phase is not necessarily much longer than the relaxation time T_1, so we cannot estimate $T_1 = \langle t \rangle$ to describe the exponential decay. Instead, we use Bayes' theorem to find the posterior distribution function of $\gamma = 1/T_1$ given the data and evaluate its maximum for estimating T_1 and its width for estimating the uncertainty of T_1.

We select all time traces that show a transition in the time interval $[t_{\mathrm{min}}, t_{\mathrm{max}}]$, where $t_{\mathrm{min}} = 1$ ms and $t_{\mathrm{max}} = t_{\mathrm{R}} - 1$ ms. The time interval of 1 ms corresponds to the detector rise time. All the remaining traces are discarded, because they are either traces with initial decays and hence wrong initialization, or traces without a decay within t_{R}. The model distribution is then

$$\mathrm{pdf}(t) = \frac{1}{\alpha(\gamma)} \mathrm{e}^{-\gamma t} \gamma \tag{1}$$

with $\gamma > 0$. The normalization constant is given by the condition

$$\int_{t_{\mathrm{min}}}^{t_{\mathrm{max}}} \mathrm{pdf}(t)\,\mathrm{d}t = \frac{1}{\alpha(\gamma)} \int_{t_{\mathrm{min}}}^{t_{\mathrm{max}}} \mathrm{e}^{-\gamma t} \gamma \mathrm{d}t = 1$$

and therefore

$$\alpha(\gamma) = \int_{t_{\mathrm{min}}}^{t_{\mathrm{max}}} \mathrm{e}^{-\gamma t} \gamma \mathrm{d}t = \mathrm{e}^{-\gamma t_{\mathrm{min}}} - \mathrm{e}^{-\gamma t_{\mathrm{max}}}.$$

From the sequence of N experimental time traces, we obtain a sequence of decay-time data of the form

$$D = \{t_1, t_2, t_3, \ldots, t_N\},$$

where N is the number of traces that showed a decay between t_{min} and t_{max}. The probability of measuring this specific dataset, if γ is known (the likelihood of the dataset D) is

$$\begin{aligned} \mathrm{prob}(D|\gamma) &= \prod_{i=1}^{N} \left(\frac{1}{\alpha(\gamma)} \mathrm{e}^{-\gamma t_i} \gamma \mathrm{d}t_i \right) \\ &= \frac{\gamma^N}{\alpha(\gamma)^N} \mathrm{e}^{-\gamma \sum_{i=1}^{N} t_i} \prod_{i=1}^{N} \mathrm{d}t_i. \end{aligned}$$

We now introduce the time average

$$\langle t_i \rangle = \frac{1}{N} \sum_{i=1}^{N} t_i.$$

This allows us to write

$$\mathrm{prob}(D|\gamma) = \frac{\gamma^N}{\alpha(\gamma)^N} \mathrm{e}^{-\gamma N \langle t_i \rangle} \prod_{i=1}^{N} \mathrm{d}t_i.$$

Using Bayes' theorem, we find the posterior distribution of γ, given a specific dataset D:

$$\mathrm{pdf}(\gamma|D) = \frac{\mathrm{pdf}(\gamma)\mathrm{prob}(D|\gamma)}{\int_0^\infty \mathrm{pdf}(\gamma)\mathrm{prob}(D|\gamma)\mathrm{d}\gamma}.$$

A suitable non-informative prior for the scaling variable γ is

$$\mathrm{prob}(\gamma) = \frac{\mathrm{d}\gamma}{\gamma}.$$

This leads us to

$$\mathrm{pdf}(\gamma|\langle t_i \rangle, N) = \frac{\frac{\gamma^{N-1}}{\alpha(\gamma)^N} \mathrm{e}^{-\gamma N \langle t_i \rangle}}{\int_0^\infty \frac{\gamma^{N-1}}{\alpha(\gamma)^N} \mathrm{e}^{-\gamma N \langle t_i \rangle} \mathrm{d}\gamma}. \tag{2}$$

This is a distribution function for γ with a sharp peak. The maximum of this distribution function gives the most probable value for γ, and its width gives the associated uncertainty.

The denominator in the posterior distribution is a constant. The numerator is a function of γ, which we define to be

$$h(\gamma) = \frac{\gamma^{N-1}}{\alpha(\gamma)^N} \mathrm{e}^{-\gamma N \langle t_i \rangle}.$$

Finding the maximum of the posterior probability density function in equation (2) amounts to finding the maximum of $h(\gamma)$. Numerically, this is most conveniently done by realizing that the maximum of $h(\gamma)$ is also the maximum of $\ln(h(\gamma))$. We find

$$\ln(h(\gamma)) = (N-1)\ln\gamma - N\ln(\alpha(\gamma)) - \gamma N \langle t_i \rangle.$$

The maximum of this function is found by solving

$$\frac{\mathrm{d}\ln(h(\gamma))}{\mathrm{d}\gamma} = \frac{N-1}{\gamma} - \frac{N}{\alpha(\gamma)}\frac{\mathrm{d}\alpha(\gamma)}{\mathrm{d}\gamma} - N\langle t_i\rangle = 0,$$

so that

$$\frac{1}{\gamma} = \frac{N}{N-1}\left(\langle t_i\rangle + \frac{1}{\alpha(\gamma)}\frac{\mathrm{d}\alpha(\gamma)}{\mathrm{d}\gamma}\right).$$

Data availability

Source data are provided with this paper. Other data supporting the findings of this study are made available via the ETH Research Collection[53].

References

50. Overweg, H. et al. Electrostatically induced quantum point contacts in bilayer graphene. *Nano Lett.* **18**, 553 (2018).
51. Wang, L. et al. One-dimensional electrical contact to a two-dimensional material. *Science* **342**, 614–617 (2013).
52. Märki, P., Braem, B. A. & Ihn, T. Temperature-stabilized differential amplifier for low-noise DC measurements. *Rev. Sci. Instrum.* **88**, 085106 (2017).
53. Garreis, R. et al. *Data Repository: Long-Lived Valley States in Bilayer Graphene Quantum Dots* (Research collection ETH Zurich, 2023); https://doi.org/10.3929/ethz-b-000635351

Acknowledgements

We thank P. Märki and T. Bähler, as well as the FIRST staff, for their technical support. We thank A. Trabesinger for his valuable input during the writing of this paper. K.E. acknowledges funding from the Core3 European Graphene Flagship Project, the Swiss National Science Foundation via NCCR Quantum Science and Technology, grant number FQXi-IAF19-07 from the Foundational Questions Institute Fund, ERC Synergy QUANTROPY number 951541, the European Union Horizon 2020 programme under grant agreement number 862660/QUANTUM E LEAPS and the EU Spin-Nano RTN network. R.G. acknowledges funding from the European Union Horizon 2020 programme under the Marie Skłodowska-Curie grant agreement number 766025. K.W. and T.T. acknowledge support from JSPS KAKENHI (grant numbers 19H05790, 20H00354 and 21H05233).

Author contributions

R.G. and C.T. contributed equally to this work. R.G. fabricated the sample. C.T. and R.G. performed the experiment with the help of W.W.H. R.G., C.T. and J.T. analysed the data with the assistance of W.W.H. and J.D.G. M.J.R. wrote the code for the pulse generation and readout with the lock-in amplifier. The pulsed measurements were set up by R.G., C.T., M.J.R., L.M.G. and W.W.H. K.W. and T.T. synthesized the hBN crystals. K.E. and T.I. supervised the project. All authors discussed the results. R.G. and C.T. wrote the paper. All authors contributed to editing the paper.

Funding

Open access funding provided by Swiss Federal Institute of Technology Zurich.

Competing interests

The authors declare no competing interests.

Additional information

Supplementary information The online version contains supplementary material available at https://doi.org/10.1038/s41567-023-02334-7.

Correspondence and requests for materials should be addressed to Rebekka Garreis or Chuyao Tong.

Peer review information *Nature Physics* thanks Björn Trauzettel and the other, anonymous, reviewer(s) for their contribution to the peer review of this work.